Effect of secondary flows due to buoyancy and contraction on heat transfer in a two-section plate-fin heat sink

I.K. Karathanassis[a, b,*], E. Papanicolaou[a], V. Belessiotis[a] and G.C. Bergeles[b]

[a]Solar & other Energy Systems Laboratory, Institute of Nuclear and Radiological Sciences & Technology, Energy and Safety, National Centre for Scientific Research DEMOKRITOS, Aghia Paraskevi, 15310 Athens, Greece

[b]Laboratory of Innovative Environmental Technologies, School of Mechanical Engineering, National Technical University of Athens, Zografos Campus, 15710 Athens, Greece

[*] Corresponding author. E-mail address: ikarathanassis@ipta.demokritos.gr (I. K. Karathanassis).

Abstract. The effect of buoyancy forces on laminar heat transfer inside a variable width plate-fin heat sink is numerically analyzed: the configuration under investigation comprises an array of rectangular fins, the number of which is doubled at the streamwise middle length of the plate, leading to a stepwise reduction in the respective channel width and hydraulic diameter. The mixed convection problem is thoroughly examined for Archimedes numbers in the range *Ar=1.32-5.82* and Reynolds numbers, based on the channel hydraulic diameter before the stepwise reduction, in the range *Re=559-667*, under the thermal boundary condition of axially constant heat flux. It is illustrated that the secondary flow pattern emanating from the flow contraction and manifested through the presence of a pair of counter-rotating horseshoe vortices and a pair of counter-rotating (fin) sidewall vortices interacts with longitudinal rolls created by buoyancy forces. In fact, the lower horseshoe vortices that are co-rotating with the buoyancy-induced rolls are significantly enhanced in magnitude and cause intense fluid mixing in the vicinity of the channel bottom wall, with a substantial distortion of the temperature field. The numerical results indicate that the joint action of the buoyancy-induced rolls and the combined secondary flow pattern has a beneficial impact on the heat sink thermal performance, a fact quantified through the circumferentially-averaged local Nusselt number distributions. The effect of the top lid thermal conductivity on the heat transfer inside the heat sink is also discussed. Finally, a comparative investigation is conducted between the present variable-channel-width configuration and two configurations of fixed-width heat sink designs. The comparative results reveal that the introduction of stepwise channels leads to superior heat transfer performance, i.e. lower values of the total thermal resistance with mitigated pressure drop penalty and increased temperature uniformity on the cooled surface.

Keywords: plate-fin heat sink, mixed convection, buoyancy rolls, longitudinal vortices, heat transfer enhancement

Nomenclature

a	wall thickness to channel width ratio $a = \frac{W_w}{W_{ch}}$
A	area, m^2
Ar_i	Archimedes number of heat-sink section i (i=1,2) $Ar_i = \frac{Gr_i}{Re_i^2}$
AR	aspect ratio $AR = \frac{H_{ch}}{W_{ch}}$
C_p	pressure coefficient $C_p = \frac{p - p_{ref}}{1/2 \rho w_i^2}$
c_p	specific heat, J/kgK
CR	concentration ratio $CR = \frac{A_{reflector}}{A_{receiver}}$
$D_{h,i}$	hydraulic diameter of heat-sink section i (i=1,2) $D_{h,i} = \frac{2W_{ch,i}H_{ch}}{(W_{ch,i} + H_{ch})}$, m
Gr_i	Grashof number of heat-sink section i (i=1,2) $Gr_i = \frac{g\beta q'' D_{h,i}^4}{\nu^2 k_f}$
H	overall heat-sink height $H = H_{ch} + t_s$, m
H_{ch}	channel height, m
h	heat transfer coefficient $h = \frac{-k(\partial T / \partial n)_w}{(T_w - T_{f,m})}$, W/m^2K
k	thermal conductivity, W/mK
L	length, m
L_Z^*	non-dimensional reattachment length $L_z^* = \frac{L_z}{W_w}$
Nu_i	Nusselt number of heat-sink section i (i=1,2) $Nu_i = \frac{h \cdot D_{h,i}}{k_f}$
p	pressure, Pa
Pr	Prandtl number $Pr = \frac{c_p \mu}{k}$
p_{ref}	pressure at the channel mid-length (L/2) for undisturbed parallel flow, Pa
Q	heat rate, W
q''	heat flux, W/m^2
Ra	Rayleigh number $Ra=GrPr$

Re_i	Reynolds number in heat-sink section i (i=1,2) $Re_i = \frac{w_{m,i} D_{h,i}}{\nu}$
R_{th}	thermal resistance, K/W
s	unwound coordinate, m
S^*	non-dimensional unwound coordinate $S^* = \frac{s - z_0}{D_{h,1}}$
T	temperature, K
t_s	solid substrate thickness, m
$\dot{V}$	volumetric flow rate, m^3/s
W	width, m
w	flow axial velocity, m/s
x,y,z	streamwise, vertical and spanwise coordinate respectively, m
X^*	non-dimensional spanwise coordinate $X^* = \frac{x}{W_{ch,2}} - \frac{1}{2}$
Y^*	non-dimensional height-wise coordinate $Y^* = \frac{y - t_s}{H_{ch}}$
Z^*	non-dimensional streamwise coordinate $Z^* = \frac{z - z_0}{D_{h,1}}$
z_0	location of the flow contraction z_0=0.25m

Greek symbols

β	volumetric thermal expansion coefficient, K^{-1}
μ	dynamic viscosity, Pa·s
ν	kinematic viscosity, m^2/s
ρ	density, kg/m^3
ω	vorticity $\vec{\omega} = \vec{\nabla} \times \vec{\upsilon}$, s^{-1}

Subscript

cal	caloric
conv	convective
cond	conductive
ch	channel
cs	cross section
f	fluid
FD	fully developed
hs	heat sink
i	inlet
init	initial
int	interface
max	maximum
ove	overall
ref	reference
s	solid, section
tot	total

w wall

1. Introduction

Heat transfer enhancement and effective heat flux dissipation are of vital importance to a significant number of engineering applications ranging from cooling of electronics and various industrial processes to concentrated solar power applications. A practice commonly employed in various heat exchanging devices, in order to increase the overall heat transfer rate, is the use of extended surfaces, such as fins or pins, with a proper geometrical layout so that the ratio of the area available for heat transfer to the overall volume of the device is maximized. An additional factor which, in many cases, leads to enhanced heat transfer is the onset of secondary flow patterns, which can arise, among others, due to the morphology of the surface geometry, the effect of buoyancy forces or by some external excitation (e.g. surface vibration) [1,2]. If the topology of these patterns is such as to allow free-stream fluid entrainment toward the heated surfaces, then the overall heat transfer rate is significantly enhanced due to the local thinning of the boundary layer and the intense thermal mixing [1]. Research in the field of heat transfer enhancement is still ongoing especially regarding heat exchanging configurations employing extended surfaces, which are the most commonly encountered in industrial applications. Various fin designs have been proposed and investigated, e.g. wavy, louvered, corrugated or offset-strip fins and a comprehensive overview of the flow and heat transfer behavior of characteristic plate-fin configurations can be found in [3,4]. Enhanced heat-transfer designs have also been proposed for layouts in the microscale [5]. In addition, techniques used for heat transfer enhancement through the prevalent flow conditions are reported in the review articles by Jacobi and Shah [2] and Bergles [6].

Two basic configurations of flow-contraction, usually found in heat dissipation applications, are the forward facing step and flow entrance into an array of parallel fins, with the latter having been primarily investigated under forced convection conditions and using air as the cooling medium [7-9]. However, few studies are available in the open literature that discuss the effect of buoyancy on heat transfer in such configurations. The published numerical and experimental results concerning laminar mixed convection over a forward-facing step are summarized in [10]. The effects of fin height and spacing on mixed-convection heat transfer around an array of longitudinal plates shrouded by a rectangular duct were in depth investigated in the experiments of Maughan and Incropera [11]. The bottom and upper duct walls were isothermally heated and cooled respectively. It was observed that for Reynolds numbers within the laminar regime and small fin height, the reduction of fin spacing reduced the overall heat transfer, despite the additional heat-transfer areas, due to the weakening of the buoyancy induced secondary vortices. However, the opposite trend was observed for fins of considerable height as the enhancement due to the extended surfaces had a decisive impact on the overall heat transfer rate. Chong et al. [12] conducted an experimental investigation of the laminar mixed convection inside a horizontal rectangular duct having a vertical longitudinal plate at the middle of its cross-section. The imposed thermal boundary condition was that of axially uniform heat flux with circumferentially constant wall temperature. The authors concluded that heat transfer was enhanced with an increase in the Reynolds number, due to the increased impact of forced convection, while duct inclination was found to have either a beneficial or a hindering influence on heat transfer, depending on the orientation of the buoyancy force in comparison to the flow direction. More recently, Dogan and

Sivrioglu [13] examined both numerically and experimentally the overall heat transfer from an array of longitudinal fins mounted inside a rectangular horizontal channel under mixed convection conditions. A constant heat flux was applied at the channel bottom wall, while the heat was dissipated through laminar air flow. The authors analyzed the effect of fin spacing and clearance gap between fin tips and the channel top surface on the average heat transfer coefficient inside the channel. They came to the conclusion that an optimal fin spacing exists that maximizes heat transfer, while a widening of the clearance gap had a negative impact on heat transfer, a trend more pronounced for larger Reynolds numbers.

Whereas the available literature referring to mixed convection in flow-contraction geometries of rectangular cross section is quite limited, many researchers have addressed the same issue in parallel flow inside straight rectangular channels. Cheng et al. [14] theoretically investigated laminar mixed convection of a large Prandtl fluid in horizontal channels under constant heat flux. They demonstrated that the buoyancy effect enhances heat transfer and reduces the thermal entry length in comparison to pure forced convection. Furthermore, they concluded that the characteristic minimum that appears in the Nusselt number distribution at the thermally developing flow region is due to the combined entry- and secondary-flow effect. Nonino and Del Giudice [15] applied a finite-element procedure to predict laminar water flow and mixed convection in a duct of aspect ratio 0.5, under asymmetrical heating on different sides of the duct by means of a uniform heat flux. In the cases of two-surface heating they observed oscillations in the local Nusselt number, which they attributed to the instability of the temperature distribution on the heated walls. Chou [16] introduced a vorticity-velocity formulation of the Navier-Stokes equations to numerically examine the effect of the circumferential heat flux distribution on the laminar mixed convective air flow in a square duct. The greatest heat transfer enhancement was found to occur for a channel where the lower symmetrical half relative to the center-plane of the cross section had conductive walls, while the upper half was kept adiabatic. In a later study, Chou [17] focused on the heating of a rectangular channel under the thermal boundary condition of axial constant heat flux with circumferentially uniform wall temperature, namely the H1 boundary condition as defined by Shah and London [18]. The author considered thermal developing flow of air and water inside horizontal channels of various aspect ratios, ranging from 0.2 to 5, and it was demonstrated that, for high Rayleigh numbers, the Nusselt number distribution exhibits two local extrema and that the local maximum value occurs close to the location of the secondary flow maximum intensity. In general, it was concluded that the secondary flow induced by buoyancy significantly enhances heat transfer.

As inferred from the above-mentioned studies, the combined effect of the different secondary flow patterns invoked by the buoyancy forces and of the geometric contraction has not been looked into, so that the thermal performance of an integrated heat exchanging device can be evaluated. The scope of the present work is, therefore, to highlight the effect of buoyancy forces on the overall heat transfer inside a plate-fin heat sink with a stepwise-varying channel width. The heat-sink configuration under investigation is primarily oriented toward concentrating solar applications. More specifically, the heat-sink has been incorporated in a parabolic trough Concentrating Photovoltaic/Thermal (CPVT) system designed by the authors [19], in order to extract useful heat from the backside of a solar cell module. Initially, the complex flow field, resulting from the combined effect of buoyancy and flow-contraction, is analyzed for increasing Archimedes or (Richardson) number. In a second stage, the influence of the combined secondary flow pattern and the circumferential wall heat flux

distribution on the overall heat transfer rate of the heat sink is quantified through distributions of the local Nusselt number. The overall performance of the variable-width (VW) heat sink is also compared to that of two similar fixed-channel-width (FW) heat sinks, obtained by considering straight channels of rectangular cross-section through the entire length, each with the width of one of the two respective sections of the VW length.

2. Geometry

The plate-fin heat-sink configuration to be addressed by the present study (Fig. 1a) has overall dimensions of (L x W) 500mm x 60mm and employs an array of rectangular channels with a step-change to their hydraulic diameter at the heat-sink mid-length. The design is based on a concept first introduced by Barrau et al. [20]. Such a concept, obtained, for instance, by the doubling of the number of channels in the downstream section, offers additional heat-transfer surfaces and disrupts the development of the cooling-fluid thermal boundary layer, which would lead to steep temperature gradients. Both these effects are expected to have a positive impact on the heat sink thermal performance; however, the presence of additional channels in the heat sink second section leads to a higher pressure-drop penalty. The channel width ratio $W_{ch,1}/W_{ch,2}$ is taken here equal to three for structural reasons, while the fin thickness W_w, which is maintained constant throughout the heat-sink length, is equal to the channel width of the second section. With respect to these geometrical constraints, the number of channels in each section can be explicitly determined through the relation:

$$N_i = \frac{W_{hs} - a_i W_{ch,i}}{(a_i + 1) W_{ch,i}} \tag{1}$$

where $\alpha = W_w/W_{ch}$ and W_{hs} is the total heat-sink width. With the above choices, it turns out that the second section consists of twelve channels and the first section of six.

Two fixed-width (FW) heat sinks (Fig. 1b-c) were used as reference cases for the characterization of the thermal and hydrodynamic performance of the VW configuration, employing twelve (high fin density-FW_h) and six (low fin density-FW_l) similar channels of rectangular cross section that run through the entire length of the heat sink, i.e., each identical to the upstream and the downstream section of the VW heat sink respectively.

3. Formulation of the numerical model.

3.1 Computational domain - thermophysical properties

It is computationally expensive to model the entire heat-sink and therefore the computational domain was truncated by taking advantage of the existing symmetries. The periodic unit cell selected (Fig. 2) comprises half of the channel cross-section of width $W_{ch,1}$ and the entire channel cross-section of width $W_{ch,2}$. The heat transfer problem is conjugate as heat conduction occurs in the solid substrate and the channel vertical walls (fins) and convection occurs in the fluid part of the domain. It has been reported by Chiang et al. [21] that the appearance of asymmetrical flow features is possible in perfectly symmetrical sudden-contraction configurations. However, the

Reynolds number considered in the present study is much lower than the critical value reported in [21] and therefore breakdown of symmetry is not expected.

The heat sink material that was selected for the present analysis is aluminum due to its high thermal conductivity (k_{al} *=237 W/mK*) and its corrosion endurance, whereas water was chosen as the cooling fluid. The properties of water in each one of the cases considered, apart from density, were regarded as constant and were evaluated at the fluid overall mean temperature $\overline{T_{f,ove}}$, which was estimated prior to the simulations through a global thermal balance to lie in the range 301.4-310.0 K. With reference to water density and in order to take into account buoyancy effects, the Boussinesq approximation was applied [22]:

$$\rho - \rho_{ref} = -\rho_{ref}\beta\left(T - T_{ref}\right) \tag{2}$$

where ρ_{ref} is a reference density evaluated at a reference temperature T_{ref} and β is water volumetric thermal expansion coefficient.

3.2 Governing equations and boundary conditions

In order to simplify the flow and heat transfer model, the following assumptions were applied [23, 24]:

(1) steady fluid flow and heat transfer,
(2) incompressible fluid,
(3) laminar flow,
(4) negligible viscous dissipation and radiative heat transfer

Based on these assumptions, the continuity, momentum and energy equations reduce to:

(continuity) $$\nabla \cdot \left(\rho \vec{V}\right) = 0 \tag{3a}$$

(momentum) $$\vec{V} \cdot \nabla\left(\rho \vec{V}\right) = -\nabla p + \nabla\left(\mu \nabla \vec{V}\right) + \Delta\rho \vec{g} \tag{3b}$$

(energy fluid) $$\vec{V} \cdot \nabla\left(\rho c_p T\right) = \nabla\left(k_f \nabla T\right) \tag{3c}$$

(energy solid) $$\nabla\left(k_s \nabla T_s\right) = 0 \tag{3d}$$

where $\vec{g} = (0, -g, 0)$. The appropriate hydrodynamic and thermal boundary conditions for the governing equations are imposed in accordance to the real operating conditions of the heat sink. A uniform velocity profile is imposed at the inlet:

$$z = 0, \qquad w = w_i, \; u = 0, \; v = 0 \tag{4}$$

while the average static pressure is taken equal to zero at the channel outlet

$$z = L, \qquad p_{ave} = 0 \tag{5}$$

A no-slip boundary condition is imposed on the fluid-wall interface:

$$u = v = w = 0 \tag{6}$$

A symmetry boundary condition (or adiabatic wall in the case of heat transfer) is applied on both the outer, parallel to the main flow, vertical planes of the domain. Furthermore, all the rest outer surfaces of the domain, apart from the bottom side, are also treated as adiabatic (Fig. 2):

$$\left.\begin{array}{l} x = 0 \\ x = \dfrac{W_w + W_{ch,1}}{2} \\ z = 0 \\ z = L \\ y = H \end{array}\right\} - k_s \frac{\partial T_w}{\partial n} = 0 \tag{7}$$

At the bottom surface, a constant heat flux is applied:

$$y = 0, \qquad -k_s \frac{\partial T_w}{\partial y} = q'' \tag{8}$$

The fluid temperature at the inlet is given, while at the outlet the temperature values are extrapolated using a constant gradient:

$$z = 0, \qquad T_f = T_i \tag{9}$$

$$z = L, \qquad \frac{\partial^2 T_f}{\partial z^2} = 0 \tag{10}$$

Finally, at the solid- fluid interface, continuity of both temperature and heat flux is imposed:

$$T_w\big|_{int} = T_f\big|_{int} \tag{11}$$

$$-k_s \left.\frac{\partial T_w}{\partial n}\right|_{int} = -k_f \left.\frac{\partial T_f}{\partial n}\right|_{int} \tag{12}$$

The set of governing equations along with the boundary conditions are solved using the finite volume based CFD package ANSYS CFX (v.13) [22]. A convergence criterion of 10^{-6} is set for the root mean square (RMS) mass, momentum and energy residuals.

3.3 Validation of the numerical model

The case of laminar mixed convection around a shrouded array of parallel fins investigated by Maughan and Incropera [11] was used in order to verify the accuracy

of the numerical scheme. The specific experimental study is the one selected among others in the open literature as bearing the closest resemblance to the present investigation. It focuses on the effect of fin spacing and fin height on the overall heat transfer rate for increasing values of the Rayleigh number. The temperature of the bottom wall and the vertical fins is maintained constant at a prescribed value T_{bot} that also determines the value of the Raleigh number, while the temperature of the top wall T_{top} is maintained constant in all cases and equal to the fluid inlet temperature ($T_{top}=293K$). The overall Nusselt number is calculated by the expression:

$$Nu = \frac{Q}{A_{bot}\left(T_{bot} - T_{top}\right)} \frac{H}{k_f} \tag{13}$$

where Q is the total heat transfer rate, A_{bot} is the unfinned area of the bottom wall and H is the distance between the bottom and the top wall.

The obtained Nusselt number values by the present numerical investigation were compared against the experimental ones for different values of the fin spacing s ($0.5 \cdot H$,$1.0 \cdot H$ and $2.0 \cdot H$) and fin height $H_f=0.9 \cdot H$. The computational domain used for the validation study is limited to half the cross-section of adjacent fins for the two larger values of the fin spacing; however, the entire cross-section between fins is used for the closest fin spacing. The Reynolds number (based on the distance H) that characterizes the flow is equal to 1000 and the Rayleigh number lies in the range $3500 \leq \mathrm{Ra} \leq 29700$. The comparative results are presented in Fig. 3 and, as can be seen, good agreement is established between the predicted and the experimental values. The maximum discrepancy detected between the comparative values is approximately equal to the minimum uncertainty of the experimental data (7%) stated by the authors, with the exception of the values regarding the highest Rayleigh number value for fin spacing $s=H$. The discrepancy in the specific case is approximately equal to 10% but, as can be detected in Fig. 3, the experimental value does not follow the evident increasing trend of the Nusselt number upon increasing Rayleigh number, indicating possibly an underestimation of the specific value during the experimental evaluation.

4. Results and discussion

The numerical results for the mixed convection inside the VW configuration are discussed in the following sections. The complex flow field is first analyzed in detail and its effect on the heat transfer performance of the heat sink is subsequently quantified by means of the local Nusselt distribution. The effect of the top lid thermal conductivity on the thermal performance of the heat sink is also discussed. At a final stage, the overall performance of the present configuration is comparatively evaluated against two FW heat-sink designs. It must be noted that, the spatial co-ordinates are presented in suitable non-dimensional forms, namely X^* (horizontal direction), Y^* (vertical direction), Z^* (streamwise direction) using respective characteristic lengths in each direction. This enables a more clear illustration of the results, as the channel cross-section extends to $0 \leq X^* \leq 1$ (after contraction) and $0 \leq Y^* \leq 1$, while $Z^*<0$ indicates upstream and $Z^*>0$ downstream locations respectively (Fig. 2).

4.1 Grid independence

The grid independence study was conducted for the case of the highest Archimedes number value ($Ar_1=5.82$) considered and for $Re_1=667$. A non-uniform hexahedral grid was employed along the flow direction for the discretization of the computational domain, as the grid was locally refined in the vicinity of the flow contraction, in order to fully capture the distinct flow features in that region. On the other hand, transversely to the flow direction the computational domain was discretized using equal hexahedral elements, as uniform grid density is required in order to resolve buoyancy induced secondary-flow patterns [15,25].

Three grids of increased density (coarse-intermediate-fine), consisting of 2.5, 3.6 and 4.6 x 10^6 elements respectively, were tested in order to ensure grid independence of the solution. An increase of the grid density from 2.5 to 3.6 x 10^6 elements produced a relative difference of 1.5% to the overall fluid pressure drop value. A further refinement caused a relative discrepancy of 0.6%; besides, the horizontal profiles of the axial velocity at $Z=0.5^*$ were almost identical for all three grids considered (Fig. 4a). Regarding heat transfer, grid refinement from the coarse to the intermediate grid caused a variation of 2.7% to the value of the overall mean Nusselt number. A further refinement produced a variation of 1.3%. In addition, the bottom wall temperature distribution at $X^*=0.5$ (Fig. 4b) was qualitatively captured by all three grids, with a maximum discrepancy between the values produced by the intermediate and the fine grid of 0.4%. Consequently, the intermediate grid, consisting of 3.6 x 10^6 elements, was proven adequately accurate for the production of the results presented below.

4.2 Flow and temperature field-Buoyancy effects

The proposed VW heat-sink configuration is intended for incorporation in a parabolic trough CPVT system. Such systems can achieve concentration ratio *CR* values reaching up to 100x [26], meaning that the typical 1-sun irradiation ($1kW/m^2$) is multiplied by a factor of 100 on the receiver (PV module) surface. The operating conditions that were initially considered for the numerical simulations refer to the CPVT system previously investigated by the authors [19]. Consequently, the imposed heat flux was gradually increased, so as to cover the entire range of achievable concentration ratios. The geometrical parameters and the operating conditions of the VW configuration are summarized in Table 1.

The non-dimensional parameter that quantifies the relative strength of free and forced convection in mixed convection flows is the Archimedes number (also referred to as the Richardson number by other authors). The flow conditions in each of the two sections *i (i*=1 or 2*)* of the variable-width configuration characterized by different hydraulic diameters, can be fully represented by the non-dimensional numbers summarized in Table 2. It should be taken in mind that the mean Archimedes number Ar_i and the corresponding Grashof number Gr_i are based on the circumferentially averaged heat flux, while the Reynolds number in each section Re_i varies for different cases, despite the fact that the flow rate is maintained constant. This is due to the variation of the fluid kinematic viscosity *v*, which is evaluated at the fluid mean temperature in each case. Nevertheless, the Reynolds number for all three cases lies well within the laminar region. Considering the values of Table 2, it is reasonable to expect that buoyancy will have a significant impact on the flow within the first section

of the heat sink where the respective buoyancy forces overpower the inertial forces in all cases.

Since two distinguishable mechanisms, i.e. buoyancy and flow-contraction, could be responsible for the emanation of recirculation patterns, a reference case has also been included in the present results, in which the effects of buoyancy forces on the flow field have been excluded ($Ar_1=Ar_2=0$), in order to specifically highlight the contraction-induced secondary flow. The distinct features of the pure (non-buoyant) forced-convection flow are summarized in Fig. 5. The ω_z-vorticity component iso-surfaces, computed for $Re_1=519$ and depicted in Fig. 5a, reveal the existence of two pairs of counter-rotating vortical structures (vortices V1-V2 and V3a-V3b), lying symmetrically about the channel horizontal mid-plane ($Y^*=0.5$). The pair V1-V2 originates at the edge between the endwalls and the fin frontal surface, while the pair V3a-V3b, which actually consists of two branches of the same vortex, is attached to the fin sidewall. The emergence of the vortices V1-V2 due to the interaction of two wall boundary layers perpendicular to one-another indicates that in fact they are a pair of horseshoe vortices [2,27]. The mechanism that causes the formation of the horseshoe vortex, as depicted in Fig. 5b, is the gradual deceleration and eventual separation of the upstream boundary layer due to the adverse pressure gradient in the contraction region. Consequently, the boundary layer initially rolls up to a cross-stream (XZ) vortex, which is entrained to the main flow, because of the spanwise pressure gradient and flows around the fin, obtaining by this way its distinct shape. The origin of the V3a-V3b vortex pair can be determined if we consider the iso-surface of the total vorticity ω, illustrated in Fig. 5c. In the present configuration, the recirculation bubble attached to the flow-contracting fin sidewall, a distinctive feature of flow separation around elongated obstacles [28,29], appears distorted towards its ends due to the influence of the endwalls and forms a hairpin-shaped vortical structure (Fig. 5c). The vortex pair V3a-V3b observed in Fig. 5a is in fact the offset of the bent ends of this hairpin vortex on a cross-flow (XY) plane. Further clarification on the topology of the contraction-induced secondary flow is available in a separate investigation conducted by the authors [30].

Considering mixed convection conditions, Fig. 6a reveals that buoyancy-induced longitudinal rolls that tend to draw fluid from the upper adiabatic wall towards the lower heated wall. are present in the first section of the heat sink even for the lowest value of the Archimedes number, $Ar_1=1.32$. The streamwise distribution of the maximum vorticity magnitude in the channel first section (Fig. 6b), away from the influence of the flow contraction, indicates that the intensity of the rolls gradually increases until a maximum intensity is reached and then decreases as the contraction location is approached. This behavior, which has also been reported by Cheng [14], is dictated by the initially high and subsequently decreasing bulk temperature difference between fluid and channel wall [14], which consequently determines the intensity of the secondary flow. The location of the maximum roll intensity is shifted towards the channel inlet as the Archimedes number increases, while for $Ar_1=5.82$ a second (local), albeit much flatter, peak in the value of the roll maximum intensity can be detected at approximately $Z^*=-9.0$.

As shown in Fig. 6b the longitudinal buoyancy rolls maintain a considerable magnitude as they approach the region of flow contraction and therefore, they interact with the contraction-induced vortical structures (shown in Fig. 5a), as depicted in Fig. 7a. The interaction of the rolls with the longitudinal vortices produces a non-symmetrical flow field in the contraction region, as becomes evident from Fig. 7b where three pairs of ω_z-vorticity iso-surfaces of equal magnitude (50-40-30 s^{-1}) and

opposite sign are plotted. The lower "modified" horseshoe vortex appears to be of considerably larger magnitude than the upper one, which is significantly shrunk in comparison to the non-buoyant case. Fig. 7b reveals that the topology of the hairpin-type vortex (branches V3a-V3b in Fig. 5) is affected by the buoyancy forces as well. The lower branch is much more localized than the upper one and furthermore it exhibits a higher intensity than its counterpart, as illustrated by the extent of the iso-surfaces of the highest ω_z-vorticity absolute value. The asymmetric topology of the hairpin vortex is primarily influenced by the distortion of the upstream velocity profile and the shift of the maximum velocity location under the channel mid-height due to the effect of buoyancy forces.

Fig. 7c presents the maximum vorticity magnitude values at a specified sampling location downstream of the contraction ($Z^*=1.0$). Both the buoyancy roll and the lower horseshoe vortex are of clockwise rotation and therefore their interaction leads to a significant enhancement of the lower longitudinal vortex, which subsequently leads to heavy fluid mixing in the vicinity of the heated bottom wall at the heat sink second section. The opposite occurs for the upper vortex, as it is counter-rotating to the respective buoyancy roll. Regarding the mixed convection cases, both vortices tend to gain in magnitude which increases in a linear manner as the Ar_1 number increases, albeit with the lower vortex exhibiting a relatively steeper increase with Ar_1. This magnitude enhancement of both vortices is, to some extent, also due to the change in thermophysical properties with the fluid mean temperature in each case. As the mean fluid temperature increases, the kinematic viscosity obtains lower values and the Reynolds number increases, consequently affecting the intensity of the longitudinal vortices (see Table 2). Nevertheless, regarding the upper vortex, the action of the buoyancy induced roll, which significantly increases in intensity with Ar_1, should cancel the effect of the increased Reynolds number. As depicted in Fig. 7d, the center of the roll moves toward the channel bottom wall as the Archimedes number increases and thus the influence of the roll on the upper vortex is mitigated to such an extent that it becomes inferior to the effect of the Reynolds number. On the other hand, the effect of the roll on the lower vortex becomes more significant for high values of the Archimedes number, a tendency that also explains the steeper increase in the magnitude of the lower vortex with Ar_1.

The topology of the fin tip separation bubble at the entrance of the second section of the heat sink is also significantly influenced by the effect of the combined secondary-flow pattern, as illustrated by the axial velocity contours on different horizontal planes, depicted in Fig. 8a. It is evident that the recirculation region has a three-dimensional non-symmetrical topology with its maximum size being located below the channel mid-height. Besides, the bubble does not cover the entire width of the fin sidewall (e.g. see contour at Y*=0.8). Fig. 8b presents the distribution of the non-dimensionalized flow reattachment length L_z^* along the channel height for the three cases examined. An initial finding is that the streamwise and cross-stream extent of the recirculation region increases with Ar_1, although its characteristic shape remains invariable. It must be noted that the reattachment length downstream of the plate tip varies linearly with the Reynolds number [29]. In the present case, as explained earlier, an increase of the Archimedes number leads to an increase of the Reynolds number as well, up to approximately 19% for the case of $Ar_1=5.82$. Although, the shape of the separation bubble is significantly affected by the combined secondary flow, the reattachment length in the region around the fin mid-height is primarily influenced by the Reynolds number. Thus, the increased Reynolds number causes a more extensive recirculation region. Additionally, it can be seen that the

recirculation bubble is completely absent for $Y^*>0.77$ and $Y^*<0.08$ in all cases. The upper part of the bubble is destroyed due to fluid stratification provoked by the buoyancy forces, while the lower part is destroyed by the lower horseshoe vortex which is of considerable size and draws high-velocity fluid towards the sidewall affecting by this way the coherence of the bubble. The decay of the recirculation bubble in regions under the influence of longitudinal vortices has also been reported by Zhang et al. [31].

It is of engineering interest, since a cooling device is investigated, to elucidate the effect of the emerging recirculation pattern to the temperature field within the variable-width configuration. Fig. 9 illustrates the temperature distribution on several cross-flow planes in the vicinity of flow contraction for the cases of Ar_1=1.32 (Fig. 9a) and 5.82 (Fig. 9b) respectively. Temperature stratification can be observed upstream of the contraction in both cases as warmer fluid is transferred towards the top of the channel due to the buoyancy forces; as expected, stratification is more intense for Ar_1=5.82. A close look at the temperature contours depicted in Fig.9 reveals that the bottom wall boundary layer in the first channel section is cooled as the flow contraction is approached (e.g. see contour plots at Z^*=-1.0 and Z^*=0.5). The cause of this distinct temperature distribution is the flow reversal occurring at the contraction region as explained in detail by the authors in [30].

Downstream of the contraction, the contour lines exhibit an intense distortion at the location of the strong lower vortex. This localized distortion is mainly due to the decreasing effect of buoyancy, which had a more global influence upstream, in the downstream section where the enhanced lower horseshoe vortex dominates. Regarding the case of Ar_1=5.82 where the distortion is more profound, a hot spot is clearly visible at the "eye" of the lower vortex increasing in size downstream (Fig. 9b). In both cases, downstream of the contraction the unheated fluid core region is pushed toward the channel top wall causing thermal energy redistribution.

Fig. 10 presents the development of the vertical temperature profiles at the center of the second-section channel (X^*=0.5) for all the cases considered. The clearly discernible linear part of the profiles ($Y^*<0$) accounts for the temperature distribution in the solid substrate. It is evident from Fig. 10a that downstream of the contraction (Z^*=1) the temperature profiles exhibit substantial changes in the fluid region right above the lower thermal boundary layer indicating the presence of overlapping layers of alternating cold and warm fluid in the lower channel region. These overlapping zones emerge due to heavy fluid mixing caused by the lower longitudinal vortex. A minor profile distortion is also evident at the symmetrical location near the top endwall. The distortion is of small scale due to the low magnitude of the upper vortex and primarily due to the imposed thermal boundary condition, as the top wall is kept adiabatic. In terms of heat transfer, the fluid mixing caused by the lower horseshoe vortex is of great significance as it disrupts the development of the thermal boundary layer on the bottom surface, where most of the heat is transferred. Figs. 10b and 10c illustrate the fact that the mixing zones extend to a considerable part into the second channel section, approximately equal to ten hydraulic diameters $D_{h,1}$. This renders their impact on the overall heat sink thermal performance significant, as will be discussed in the following section.

4.3 Local Nusselt number distribution

In the present study, the circumferentially averaged Nusselt number, calculated by using the values of the local heat flux and the temperature distributions available from

the numerical simulations, is selected as suitable to quantify heat transfer. The definition of the Nusselt number is based on the hydraulic diameter of each heat sink section (i=1,2):

$$\overline{Nu_i}(z) = \bar{h}(z)\frac{D_{h,i}}{k_f} \tag{14}$$

where k_f is the fluid thermal conductivity and $\bar{h}(z)$ is the local average convective heat transfer coefficient:

$$\bar{h}(z) = \frac{\bar{q}(z)}{\overline{T_w}(z) - \overline{T_f}(z)} \tag{15}$$

whereas $\bar{q}(z)$ and $\overline{T_w}$ are the circumferentially averaged heat flux and bottom wall temperature values, respectively. $\overline{T_f}(z)$ is the local fluid bulk mean (mixing cup) temperature defined as:

$$\overline{T_f} = \frac{1}{\bar{w}A_{ch,cs}} \int_{A_{ch,cs}} w(x,y)T(x,y)dA_{ch,cs} \tag{16}$$

with $\bar{w}$ the mean flow velocity inside the channel and $A_{ch,cs}$ the channel cross section.

Fig. 11a presents the values of the average local Nusselt number along the flow direction for the three cases of increasing Archimedes number. The pure forced convection results ($Ar_1=0.00$) are also presented for the sake of comparison. Regarding the first heat-sink section, heat transfer is significantly enhanced due to buoyancy as the local Nusselt values attained are much higher than the corresponding ones for forced convection and with a much flatter distribution. The enhanced heat transfer is explained, if the secondary flow pattern is considered, which is responsible for the continuous feeding of the heated bottom wall with cold fluid from the channel top part. Downstream of the contraction ($Z^* \geq 0$), the Nusselt number values obtained under mixed convection conditions are considerably higher than the respective ones for forced convection, despite the minor effect of buoyancy in the second section. It has been established that the lower longitudinal vortex gains in magnitude as the Archimedes number increases (see Fig. 7c) and this causes a more intense fluid mixing in the region of the bottom boundary layer, leading to increased heat transfer.

It is also evident from Fig. 11a that the distributions in the mixed convection cases exhibit a characteristic local minimum point at axial locations of the first section which tend to shift toward the channel inlet as the Archimedes number increases. This local minimum results from the combined effect of thermal entrance and buoyancy induced secondary flow [14,17], manifesting the strong interrelation between heat transfer and secondary flow pattern, given that the buoyancy rolls obtain their maximum magnitude (see Fig. 6b) slightly downstream of the location of the minimum Nusselt number. Downstream of the location of the minimum Nusselt number point, a region of slightly increasing Nusselt number values is detected, which extends up to approximately $Z^*=-4$. This increasing trend is due to the well established recirculation pattern, which enhances heat transfer and hence, for a

constant heat flux, decreases the wall-fluid temperature difference, as depicted in Fig. 11b. In the vicinity and immediately upstream of the flow contraction, a decrease in Nusselt number, attributed to flow separation upstream of the additional fin frontal surface, is observed, followed by a significant heat transfer rate augmentation at the location of the step-change reduction of the hydraulic diameter. Fig. 11c presents the local Nusselt number variation as a function of the non-dimensional "unwound" coordinate $S^* = \frac{s - z_0}{D_{h,1}}$, in the sense that the *s* coordinate follows the unit cell outline at the contraction region so as to include the fin frontal surface. It is evident that the local Nusselt number exhibits its peak value exactly at the symmetry line of the fin and maintains very high values throughout the fin frontal surface. This abrupt heat transfer enhancement is due to the flow impingement on the leading surface of the additional fin and furthermore to the action of the lower horseshoe vortex which draws cold free-stream fluid toward the fin (heated) frontal surface.

In order to illustrate the effect of the top lid conductivity on the heat sink thermal performance two kinds of heating conditions were considered, which can be practically realized by using a top lid of either low (e.g. Pyrex glass) or high (e.g. aluminum) thermal conductivity respectively. The computational domain representative of the latter case (four heated surfaces) includes an additional solid domain characterized by the same thermal conductivity ($k_{al}=237$ *W/mK*) as the rest of the heat sink body at the top part. Fig. 12 depicts the ratio of the Nusselt number values for the two different heating conditions considered. As illustrated, the use of an insulating top cover enhances heat transfer throughout the heat sink and especially in the first section where fluid from the top part of the channel is entrained into the lower thermal boundary layer. If the channel top surface is kept adiabatic, fluid of lower temperature is drawn toward the bottom wall due to the absence of a top thermal boundary layer, as illustrated by the inset of Fig. 12. Consequently, the use of an insulating top lid is favorable in terms of thermal performance.

4.4 Comparison to fixed-width channel heat sinks

Two FW heat sinks of the same overall dimensions, having identical fin density to the first (low-fin density, hereafter called FW_l) and the second (high-fin density, called FW_h) section of the VW design respectively, were used as reference cases for comparison, in order to evaluate the overall performance. As mixed and forced convection conditions are expected to prevail in the FW_l and the FW_h heat sinks respectively, the case of Archimedes number $Ar_{1}=1.32$ was selected for the comparative study, where the inertial and buoyancy forces are nearly counterbalanced. All the operating parameters and overall dimensions were considered the same for all three configurations, whereas the evaluation was based on the criteria of thermal resistance, pressure drop and temperature uniformity over the cooled surface. It was regarded as more suitable to perform the comparative investigation on the basis of fixed operating parameters only, rather than perform a constrained analysis regarding the evaluation criteria such as in [32]. Allowing non-constrained variation of all the evaluation quantities offers a more comprehensive illustration of the effect of the configuration geometry separately on the thermal (reflected through thermal resistance and temperature uniformity) and the hydrodynamic performance (reflected through pressure drop), respectively.

The overall thermal resistance of a heat sink configuration can be determined considering the equivalent resistance circuit [33]:

$$R_{tot} = R_{cond} + R_{cal} + R_{conv} \tag{17}$$

The three terms on the right hand side of Eq. (17) correspond to the conductive, caloric and convective individual resistances and are defined according to the following relations:

$$R_{cond} = \frac{t_s}{k_s A} \tag{18}$$

$$R_{cal} = \frac{1}{\rho \dot{V}_{tot} c_p} \tag{19}$$

$$R_{conv} = \frac{1}{\overline{h_{ove}} A} = \frac{1}{\overline{h_{ove}} \left[N \left(2\eta_{fin} H_{ch} + W_{ch} \right) L \right]}, \qquad \eta_{fin} = \frac{\tanh\left(m H_{ch} \right)}{m H_{ch}} \tag{20}$$

and $m = \sqrt{2\overline{h_{ove}} / k_s W_w}$ is the fin parameter. The overall convective resistance of the VW configuration results as the harmonic mean of the individual resistances of each section [22], i.e. connection in parallel is assumed. An alternative definition for the thermal resistance has also been proposed [34]:

$$R_{th} = \frac{T_{max} - T_{f,i}}{Q} \tag{21}$$

where Q is the overall heat rate. In the case of straight-channel heat sinks where the wall-fluid temperature difference remains constant the two definitions are equivalent. However, this does not apply for the VW configuration as the thermal resistance using Eq. (17) is calculated by taking into account the mean wall temperature (through the overall heat transfer coefficient), while the maximum wall temperature is used in Eq. (21). The induced pressure drop Δp is simply defined as the pressure difference between the outlet and the inlet, while the temperature uniformity is properly quantified through the standard deviation of the temperature values at the bottom wall.

Table 3 presents comparative results concerning the previously mentioned evaluation factors for the three heat sink designs. It must be noted that the thermal resistance of the VW configuration is calculated using both Eqs. (17) and (21). The values of Table 3 point out that the FW_1 configuration exhibits superior performance with respect to cooling-fluid pressure drop, as expected. In the FW_1 design, channels of the large hydraulic diameter $D_{h,1}$ run through the entire heat sink length and consequently the mean flow velocity is lower in comparison to the other two configurations. It is thus inevitable for the overall pressure drop to have the lowest value [35].

On the other hand, the VW configuration is superior in terms of thermal resistance and temperature uniformity. It is interesting to notice in Table 3 that the thermal

resistance value calculated by Eq. (21) is higher than the respective calculated by Eq. (17), as it is explicitly determined by the maximum temperature obtained in the first section of the heat sink, which has a moderate thermal performance. The value produced by Eq. (17) is lower as the second section of high thermal performance is also taken into account.

Fig. 13a presents the Nusselt number distributions for the two FW configurations. Regarding the FW_h design, the distribution indicates pure forced convection conditions and the fully developed value is in agreement with the theoretical prediction. Heat transfer appears more enhanced in the FW_l configuration due to the effect of buoyancy and, as can be seen from Fig. 13a, the Nusselt number values after reaching the characteristic minimum point, exhibit a slightly increasing trend. This behavior is indicative of the fact that the flow does not reach full thermal development until the outlet of the heat sink. However, the Nusselt number values can be misleading due to the use of a different hydraulic diameter in each case. The distribution of the heat transfer coefficient (Fig. 13b), which is independent of the geometrical parameters, reveals that heat transfer is significantly enhanced in the second section of the VW configuration due to the action of the horseshoe vortices. The overall convective thermal resistance of the VW configuration obtains the lowest value in comparison to the other configurations, due to the high thermal performance of its second section aided by the beneficial effect of buoyancy forces in the first section which mitigates the thermal resistance penalty associated to the use of wider channels. Finally, the more uniform temperature distribution is justified considering the interdependence between the local wall temperature and the heat transfer rate. As the heat transfer rate is constant in almost the entire length of the FW configurations, the wall temperature rises monotonically, whereas the reduction of the hydraulic diameter in the VW configuration leads to an abrupt enhancement of the heat transfer rate (see Fig. 13b) and improves temperature uniformity.

In general, the incorporation of a high-fin density second section greatly enhances heat transfer in comparison to an initially optimized, single section, low-fin density configuration and furthermore improves temperature uniformity at the substrate. Vice versa, the incorporation of a low-fin density first section induces a mitigated pressure-drop penalty in comparison to an optimized, high fin-density layout with straight fins occupying the entire length of the heat sink.

5. Conclusions

The effect of buoyancy on flow and heat transfer inside a plate-fin heat sink incorporating channels of stepwise varying width was investigated by means of a three-dimensional numerical model. It was illustrated that the geometrical contraction at the heat sink mid-length induces the onset of a symmetrical pair of longitudinal horseshoe vortices near the channel endwalls and of a hairpin type of vortex attached to the fin sidewall. In the heat sink section upstream of the contraction, two counter-rotating buoyancy rolls were detected spanning across the channel cross section. The most important consequence of the roll interaction with the contraction-induced secondary flow is the considerable enhancement of the lower horseshoe vortex. The magnitude of the lower vortex is of great significance with respect to heat transfer, as it causes intense fluid mixing in the vicinity of the bottom wall, which is the main heat transfer surface. The transversal recirculation bubble downstream of the fin tip is also greatly influenced by the action of the longitudinal vortices and obtains a non-symmetrical form with the maximum reattachment length located toward the channel

bottom wall, while its coherence is totally destroyed for $Y^*<0.08$ and $Y^*>0.77$ in all cases.

The emerging combined secondary flow greatly enhances heat transfer as the achieved Nusselt number values are considerably higher than the ones for pure forced convection. The main mechanism responsible for this enhancement is the constant feeding of the bottom thermal boundary layer with cold water from the channel core that is conducted by the buoyancy rolls in the first section and by the lower horseshoe vortex in the second section. It was also found that the presence of an upper boundary layer, in the case where a conductive top lid is used, has an adverse effect on thermal performance.

Finally, the comparative study of variable and fixed-width designs demonstrated that the introduction of stepwise varying channels is an effective way to increase the thermal performance of a heat-sink configuration without introducing a severe pressure drop penalty or conversely to mitigate the induced pressure drop without deteriorating the thermal performance.

Acknowledgments

The simulations were performed using the Cloud Computing infrastructure of the National Technical University of Athens (NTUA) computer center. The computer center staff is gratefully acknowledged for the disposed storage space and technical support. This work was financially supported by the NTUA Special Account for Research.

References

[1] T. Ota, A survey of heat transfer in separated and reattached flows, Appl. Mech. Rev. 35 (2000) 219-235.

[2] A.M. Jacobi, R.K. Shah, Heat transfer surface enhancement through the use of longitudinal vortices: A review of recent progress, Exp. Therm. Fluid Sci. 11 (1995) 295-309.

[3] R.M. Manglik, Heat transfer enhancement, in: A. Bejan, A.D. Kraus (Eds.), Heat Transfer Handbook, Wiley, New Jersey, 2003, pp. 1059-1067

[4] R.L. Webb, N.H. Kim, Principles of Enhanced Heat Transfer, second ed., Taylor & Francis, New York, pp. 89-129.

[5] S. Kandlikar, Single-phase liquid flow in minichannels and microchannels, in: S. Kandlikar, S. Garimella, D. Li, S. Colin, M.R. King (Eds.), Heat Transfer and Fluid Flow in Minichannels and Microchannels, Elsevier, Oxford, 2006, pp. 118-121.

[6] A.E. Bergles, Heat transfer enhancement- The encouragement and accommodation of high heat fluxes, J. Heat Transfer 119 (1997) 8-19.

[7] N. Djilali, Forced laminar convection in an array of stacked plates, Num. Heat Transfer, Part A, 25 (1994) 393-408.

[8] M. Rahnema, M.A. Yaghoubi, H. Kazeminejad, A numerical study of convective heat transfer from an array of parallel blunt plates, Int. J. Heat Fluid Flow 18 (1997) 430-436.

[9] M. Yaghoubi, E. Velayati, Conjugate heat transfer from surface-mounted finite blunt plates, Proc. I. Mech. Eng. Part C: J. Mech. Eng. Sci. 220 (2006) 83-94.

[10] H.I. Abu-Mulaweh, A review of research on laminar mixed convection flow over backward- and forward facing steps, Int. J. Therm. Sci. 42 (2003) 897-909.

[11] J.R. Maughan, F.P. Incropera, Mixed convection heat transfer with longitudinal fins in a horizontal parallel plate channel: Part II-Experimental results, J. Heat Transfer 112 (1990) 619-624.

[12] D. Chong, J. Liu, J. Yan, Z. Zhou, Experimental investigation of mixed convection in a rectangular duct with a heated plate in the middle of cross section., Heat Mass Transfer 43 (2007) 1283-1291.

[13] M. Dogan, M. Sivrioglu, Experimental and numerical investigation of clearance gap effects on laminar mixed convection heat transfer from fin array in a horizontal channel- A conjugate analysis, Appl. Therm. Eng. 40 (2012) 102-113.

[14] K.C. Cheng, S.W Hong, G.J. Hwang, Buoyancy effects on laminar heat transfer in the thermal entrance region of horizontal rectangular channels with uniform heat flux for large Prandtl number fluid, Int. J. Heat Mass Transfer 15 (1972) 1819-1836.

[15] C. Nonino, S. Del Giudice, Laminar mixed convection in the entrance region of horizontal rectangular ducts, Int. J. Num. Meth. Fluids, 13 (1991) 33-48.

[16] F.C. Chou, Effect of non-uniform heating on laminar mixed convection in the entrance region of horizontal ducts, Comp. Fluids 17 (1989) 487-496.

[17] F.C. Chou, Laminar mixed convection in the thermal entrance region of horizontal rectangular channels with uniform heat input axially and uniform wall temperature circumferentially, Can. J. Chem. Eng. 68 (1990) 577-584.

[18] R.K. Shah, A.L. London Laminar Flow Forced Convection in Ducts: a Source Book for Compact Heat Exchangers, Academic press, New York, 1978.

[19] I.K. Karathanassis, E. Papanicolaou, V. Belessiotis, G.C. Bergeles, Design and optimization of a micro heat sink for Concentrating/Photovoltaic Thermal (CPVT) systems, Appl. Therm. Eng., In Press.

[20] J.Barrau, D. Chemisana, J. Rosell, L. Tadrist, M. Ibañez, An experimental study of a new hybrid jet impingement/micro-channel cooling scheme, Appl. Therm. Eng. 30 (2010) 2058-2066.

[21] T.P. Chiang, A. Sau, R.R. Hwang, Asymmetry and bifurcations in three-dimensional sudden-contraction channel flows, Phys. Rev. E 83 (2011) art. no. 046313.

[22] ANSYS Inc., ANSYS CFX-Solver theory guide, Release 13.0, Canonsburg, PA 2010.

[23] P.S. Lee, S.V. Garimella, Thermally developing flow and heat transfer in rectangular microchannels of different aspect ratios, Int. J. Heat Mass Transfer 49 (2006) 3060-3067.

[24] Z. Li, X. Huai, Y. Tao, H.Chen, Effects of thermal property variations on the liquid fluid and heat transfer in microchannel heat sinks, Appl. Therm. Eng. 27 (2007) 2803-2814.

[25] A. Benderradji, A. Haddad, R. Taher, M. Médale, C. Abid, F. Papini, Characterization of fluid flow patterns and heat transfer in horizontal channel mixed convection, Heat Mass Transfer 44 (2008) 1465-1476.

[26] D. Chemisana, Building integrated concentrating photovoltaics: A review, Ren. Sust. Energy Rev. 15 (2011) 603-611.

[27] R.L. Simpson, Junction flows, Annu. Rev. Fluid Mech. 33 (2001) 415-443.

[28] K. Sasaki, M. Kiya, Three dimensional vortex structures in a leading-edge separation bubble at moderate Reynolds numbers, J. Fluids Eng. 113 (1991) 405-410.

[29] J.C. Lane, R.I. Loehrke, Leading edge separation from a blunt plate at low Reynolds number, J. Fluids Eng. 102 (1980) 494-496.

[30] I.K. Karathanassis, E. Papanicolaou, V. Belessiotis, G.C. Bergeles, Three-dimensional flow effects on forced convection heat transfer in a channel with stepwise-varying width, Int. J. Therm. Sci., In Press.

[31] L.W. Zhang, S. Balachandar, D.K. Tafti, Effects of intrinsic three dimensionality on heat transfer and friction loss in a periodic array of parallel plates, Num. Heat Transfer: Part A 31 (1997) 327-353.

[32] P. Canhoto, A.H Reis, Optimization of forced convection heat sinks with pumping power requirements, Int. J. Heat Mass Transfer 54 (2011) 1441-1447.

[33] A. Kraus, A. Bar-Cohen, Thermal Analysis and Control of Electronic Equipment, McGraw-Hill, New York, 1983.

[34] D. Liu, S.V. Garimella, Analysis and optimization of the thermal performance of microchannel heat sinks, Int. J. Num. Methods for Heat Fluid Flow 15 (2005) 7-26.

[35] R.D. Blevins, Applied Fluid Dynamics Handbook, Van Nostrand Reinhold Company, New York, 1984.

Tables

Table 1
Geometrical and operational parameters for the VW configuration.

Overall length (mm)	500.0
Overall width (mm)	60.0
1st section channel width (mm)	7.2
Number of channels - 1st section (-)	6
2nd section channel width (mm)	2.4
Number of channels - 2nd section (-)	12
Channel height (mm)	14.4
Fin thickness (mm)	2.4
Substrate thickness (mm)	3.0
Total volumetric flow rate (ml/s)	30
Heat flux density (kW/m^2)	28.3-60.0-100.0

Table 2
Non-dimensional numbers for each heat-sink section *i* characterizing the examined cases.

	Re		**Gr**		**Ar**	
q'' [kW/m^2]	***i=1***	***i=2***	***i=1***	***i=2***	***i=1***	***i=2***
28.3	559	359	4.11E+05	8.66E+03	1.32	0.07
60.0	605	389	1.14E+06	2.37E+04	3.12	0.16
100.0	667	429	2.59E+06	5.29E+04	5.82	0.29

Table 3
Comparative results for the different heat sink designs.

q'' [kW/m^2]	$\dot{V}_{tot}$ [ml/s]		**R_{th} [K/W]**	**Δp [Pa]**	**Temperature Std [K]**
28.3	*30.0*	**FW_h**	0.0184	74.34	2.304
		FW_l	0.0257	10.79	2.137
		VW	0.0166 (Eq. 17) 0.0179 (Eq. 21)	45.71	2.059

Figures

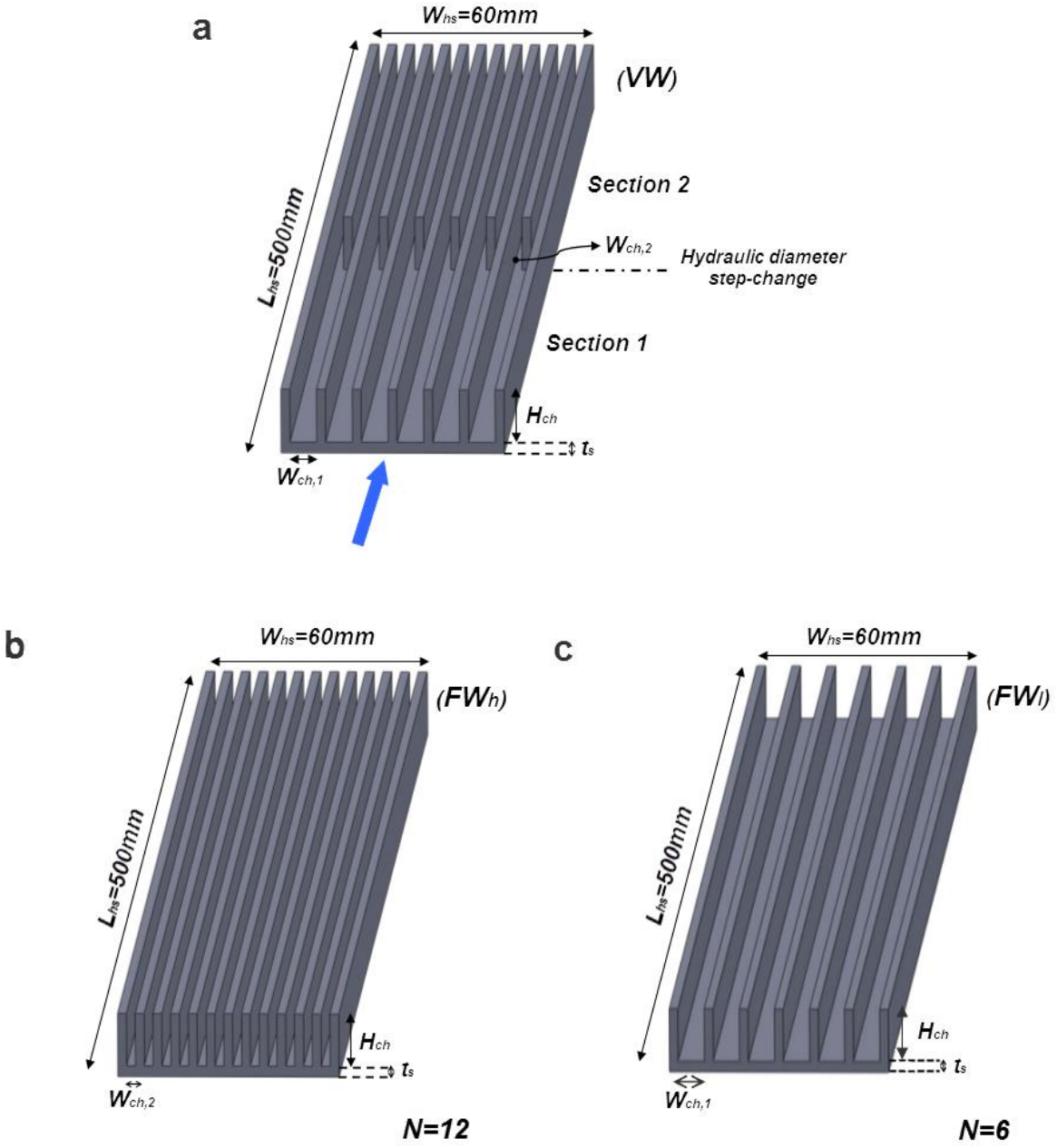

Fig. 1. The plate-fin heat sink configurations under investigation in the present study: (a) variable width (VW), (b) high fin density fixed width (FW_h), (c) low fin density fixed width (FW_l).

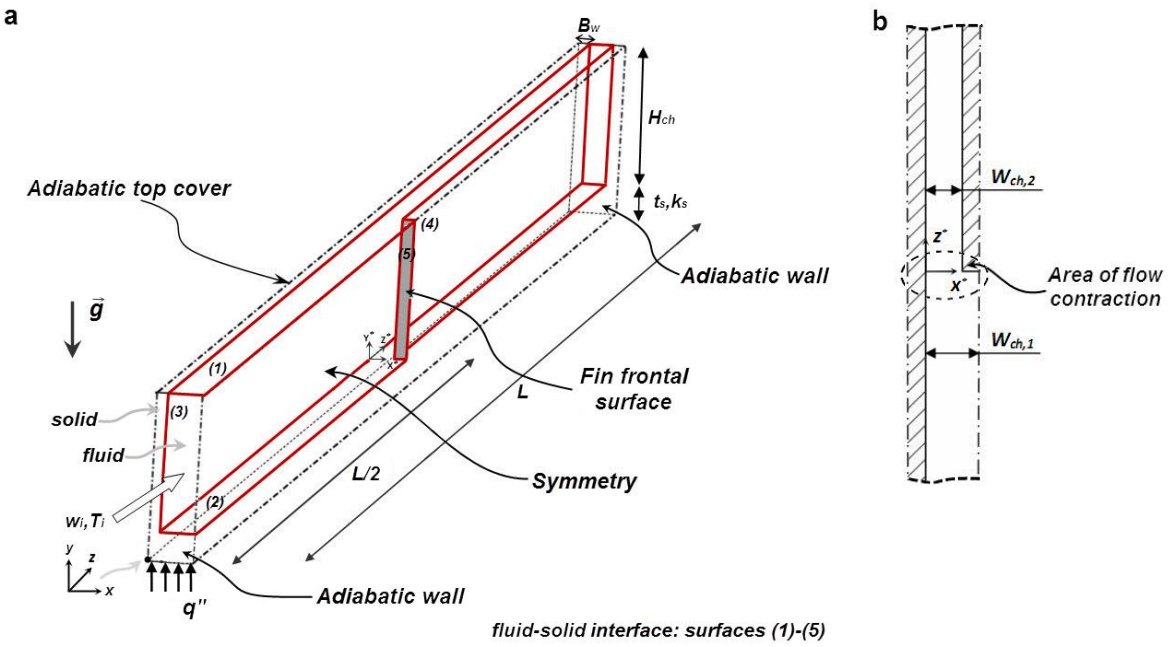

Fig. 2. Computational domain for the numerical model: (a) Perspective view, (b) top detailed view of the flow-contraction region.

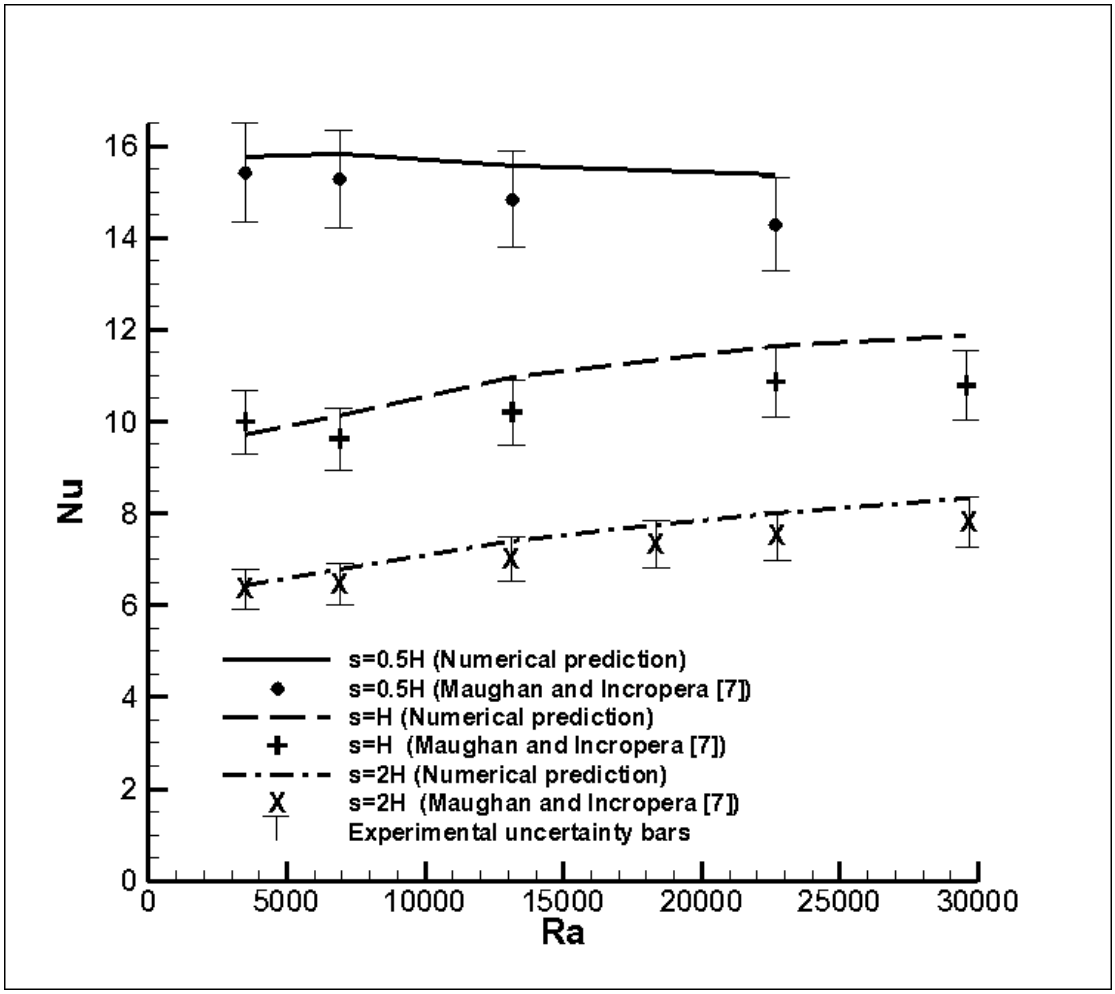

Fig. 3. Validation of the numerical code with the experimental results of Ref. **[7]** for a shrouded array of parallel fins: Computed overall Nusselt number values for Re=1000 and increasing Rayleigh number.

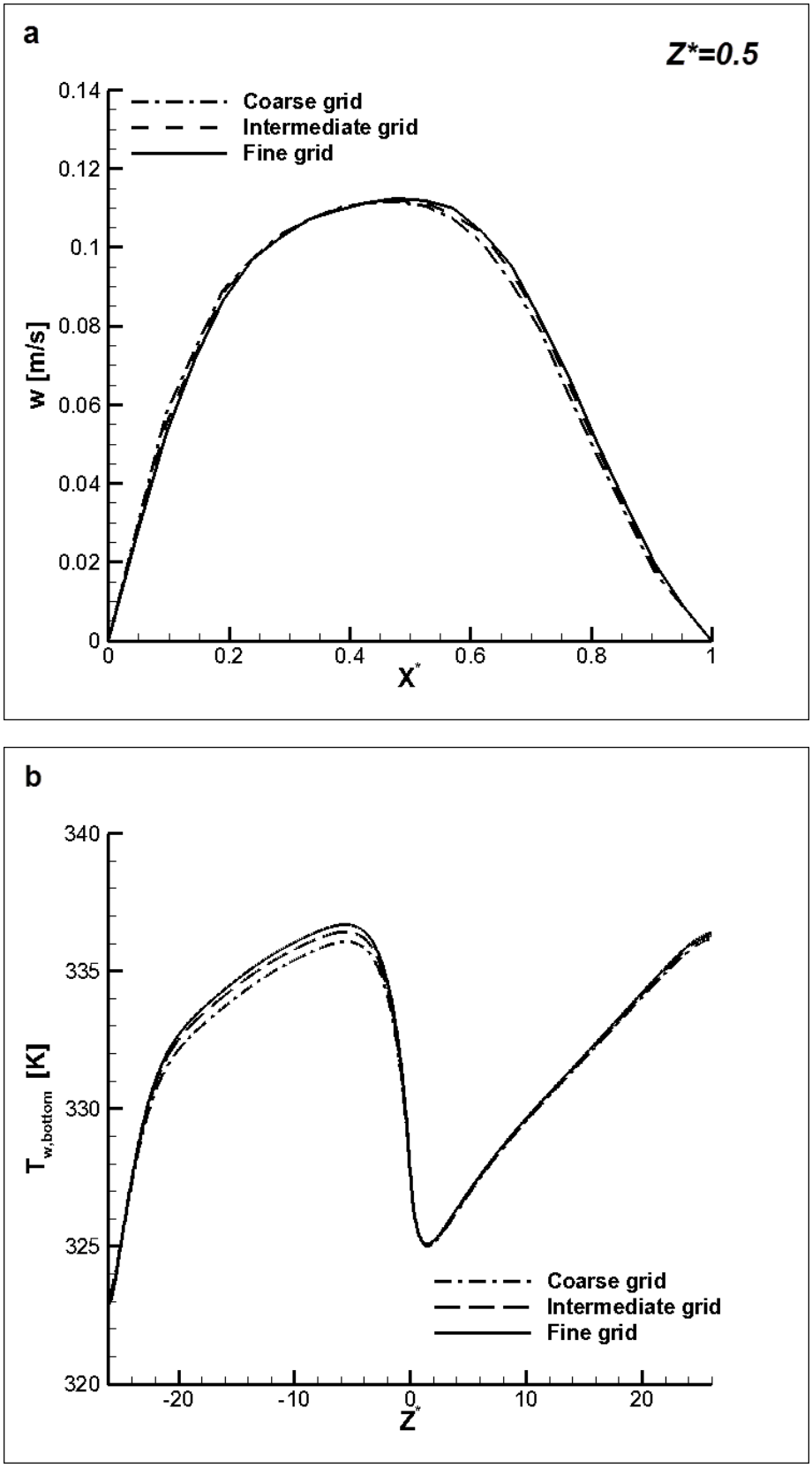

Fig. 4. Grid independence study for Ar_1=5.82 and Re_1=667: (a) Horizontal velocity profile (Y^*=0.5) at Z^*=0.5, (b) bottom wall temperature distribution at X^*=0.5 (centerline of the second section channel).

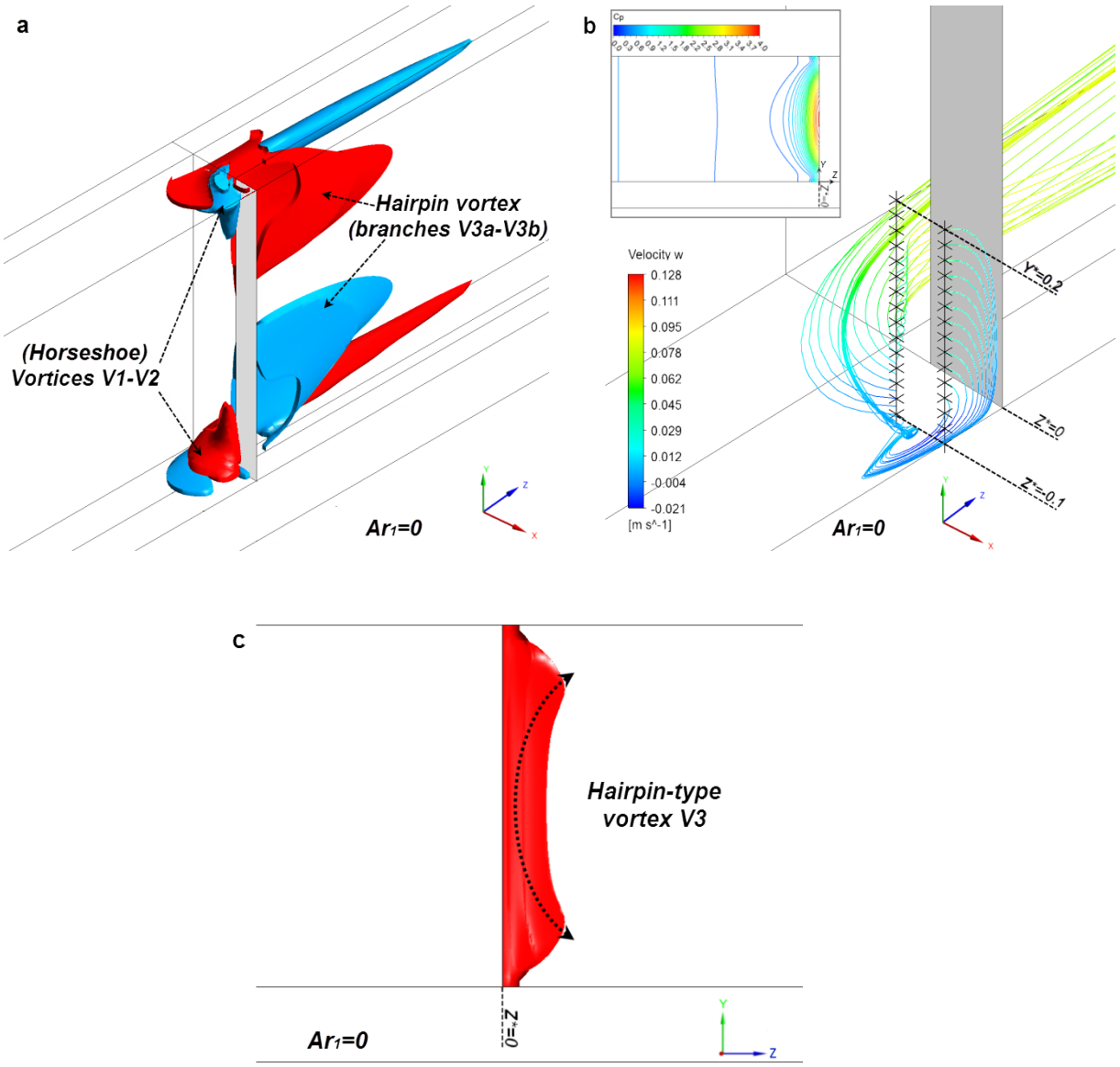

Fig. 5. (a) Results for non-buoyant flow at Re_1=519: Iso-surfaces of the ω_z -vorticity component ($|\omega_z|$=10s^{-1}) in the flow-contraction region (red-clockwise rotation, blue-anticlockwise rotation), (b) Three-dimensional streamlines originating from seed points at X^*=1.42 and X^*=1.5, respectively and (c) iso-surface of the total vorticity magnitude ($|\omega|$=200s^{-1}).

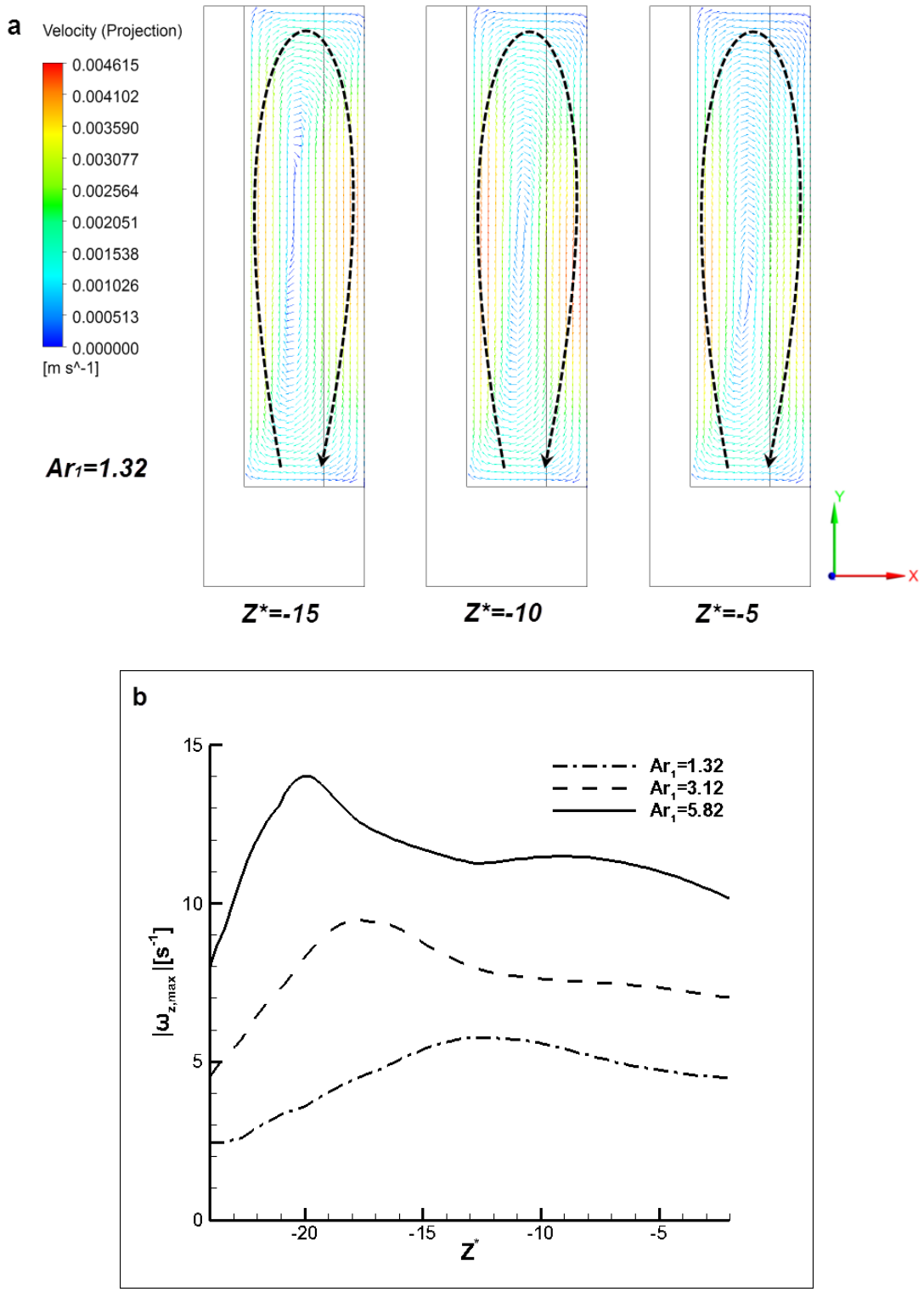

Fig. 6. Buoyancy-induced secondary flow: (a) Velocity vector plot indicating the presence of a longitudinal roll in the half cross section of the first-section channel, (b) Distribution of the roll maximum vorticity magnitude in the first section of the heat sink.

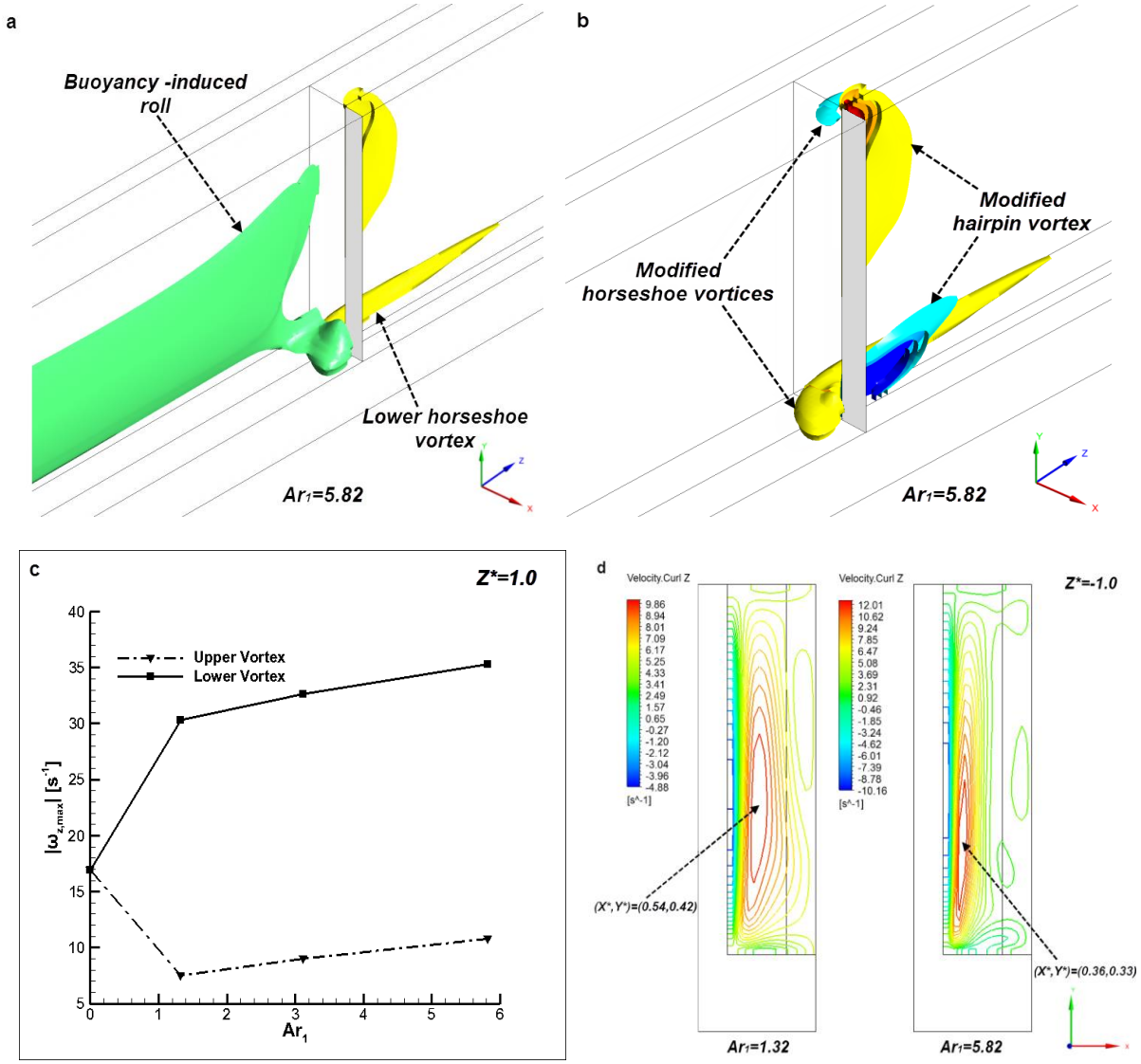

Fig. 7. Vortical structures obtained for mixed convection at Re_1=559: (a) ω_z -vorticity iso-surfaces ($\omega_{z,\ vortex}$=30s^{-1}, $\omega_{z,\ roll}$=8s^{-1}), (b) ω_z -vorticity iso-surfaces in the contraction region, (c) maximum intensity of the longitudinal vortices at Z^*=1 vs. Ar_1, (d) ω_z –vorticity contours at Z^*=-1.0.

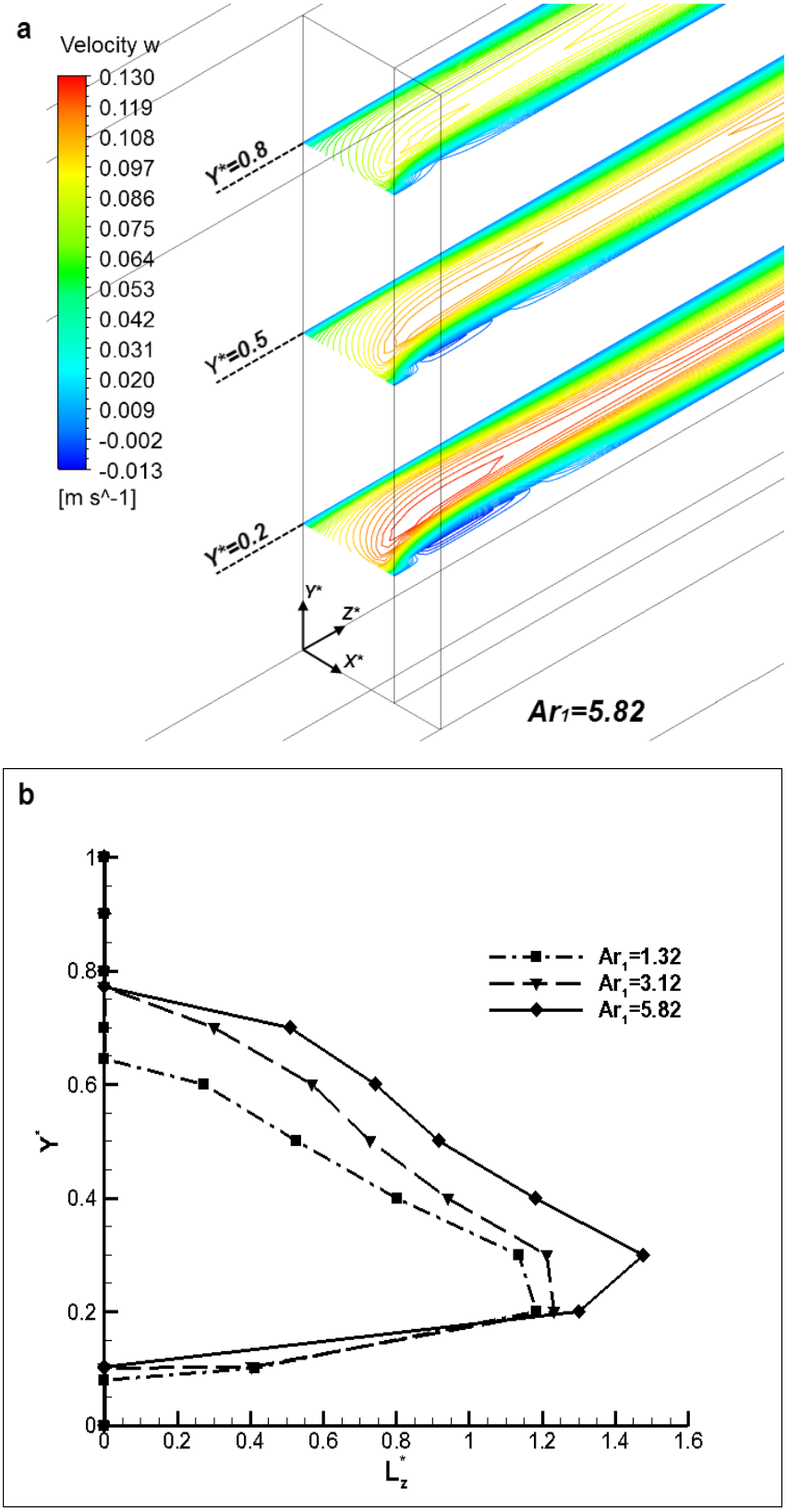

Fig. 8. (a) Axial velocity contours at horizontal planes downstream of the flow contraction, (b) Distribution of the reattachment length along the channel height.

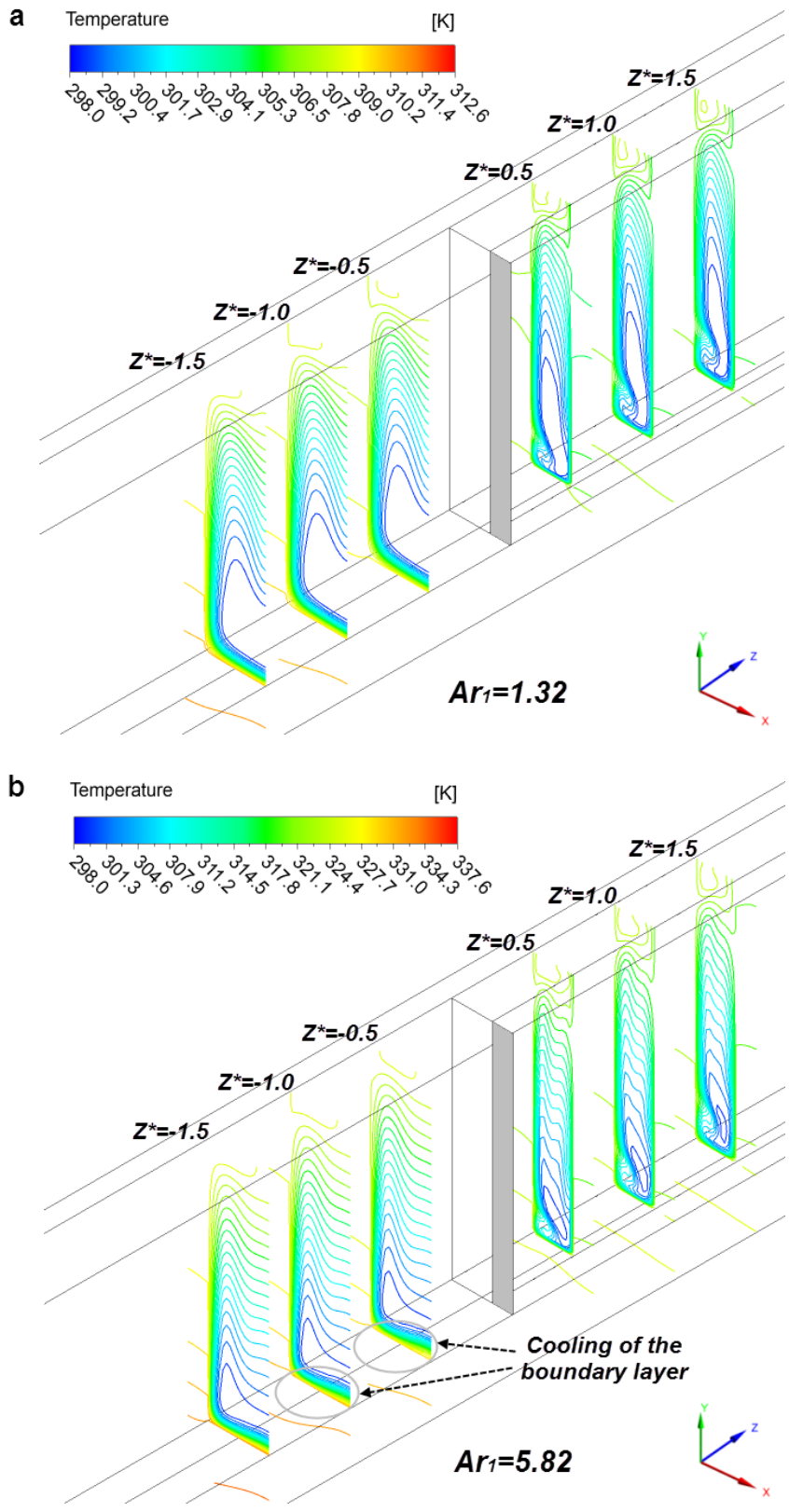

Fig. 9. Temperature contour plots at cross-flow planes of increasing streamwise coordinate in the vicinity of the flow contraction: (a) Ar_1=1.32, (b) Ar_1=5.82.

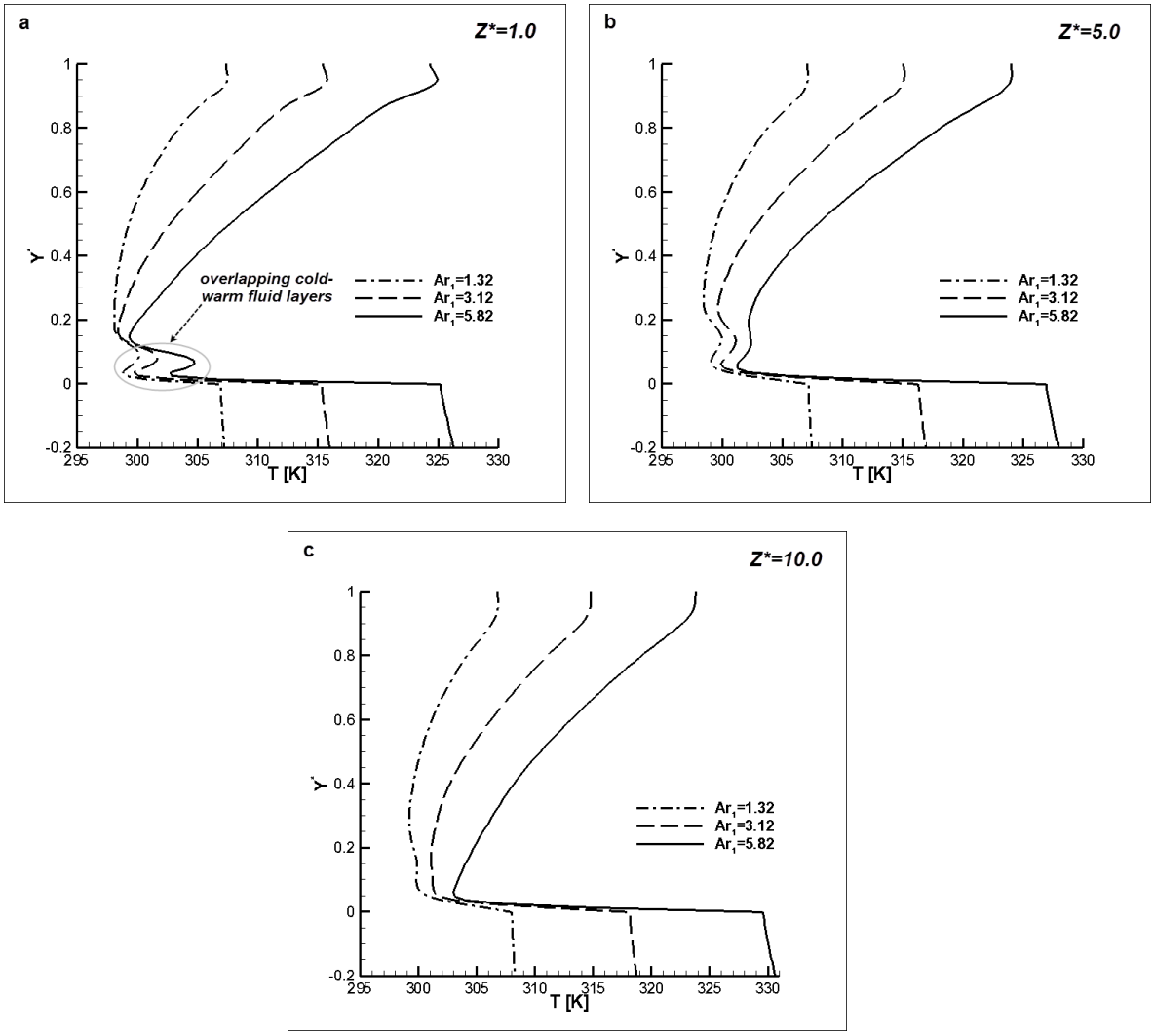

Fig. 10. Temperature vertical profile development along the flow direction at X^*=0.5. Heat sink second section: (a) Z^*=1.0, (b) Z^*=5.0 and (c) Z^*=10.0

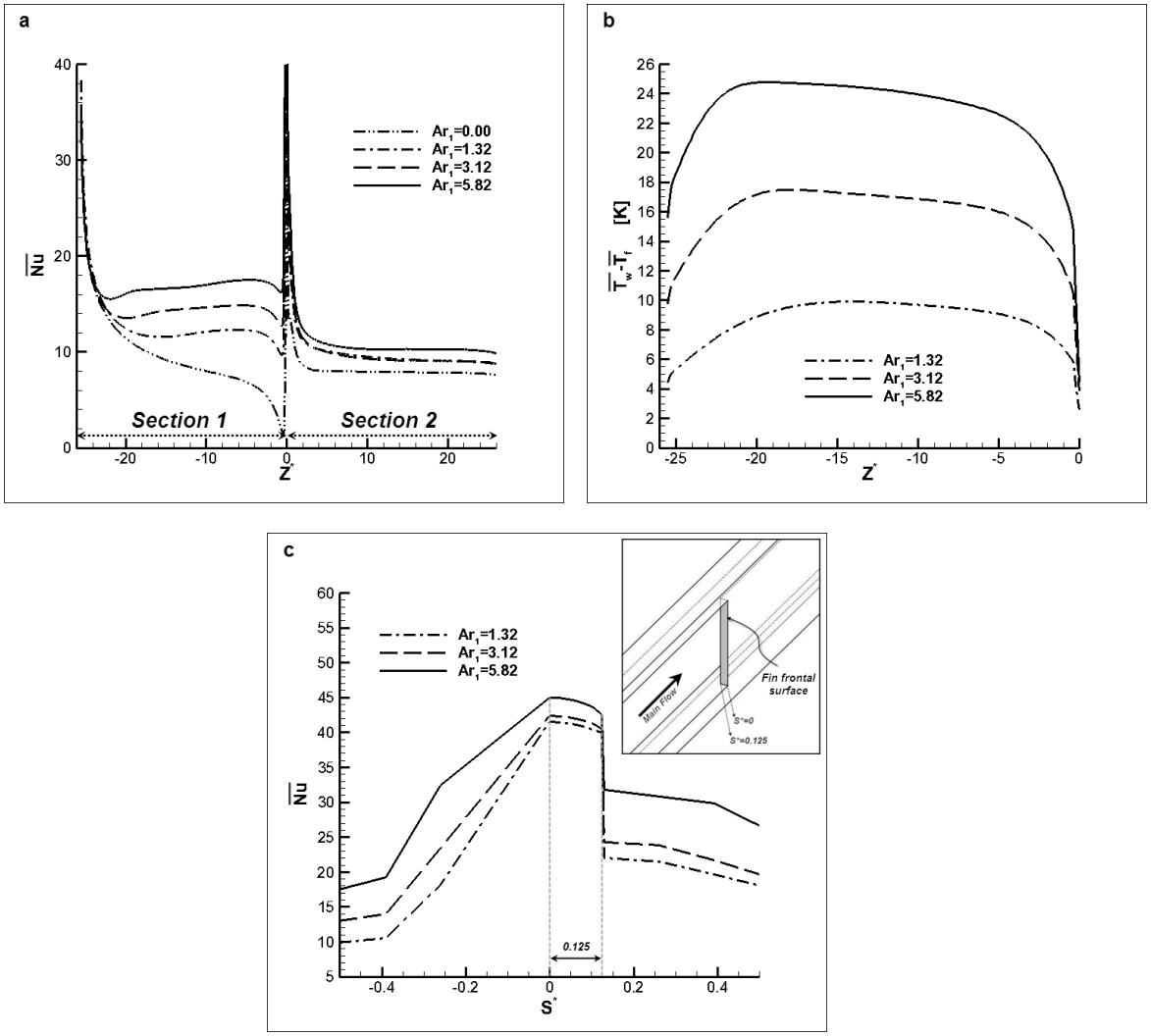

Fig. 11. (a) Distribution of the circumferentially averaged Nusselt number in the streamwise direction, (b) average wall-fluid temperature difference in the first heat-sink section and (c) local Nusselt number variation in the vicinity of the flow contraction as a function of the unwound coordinate

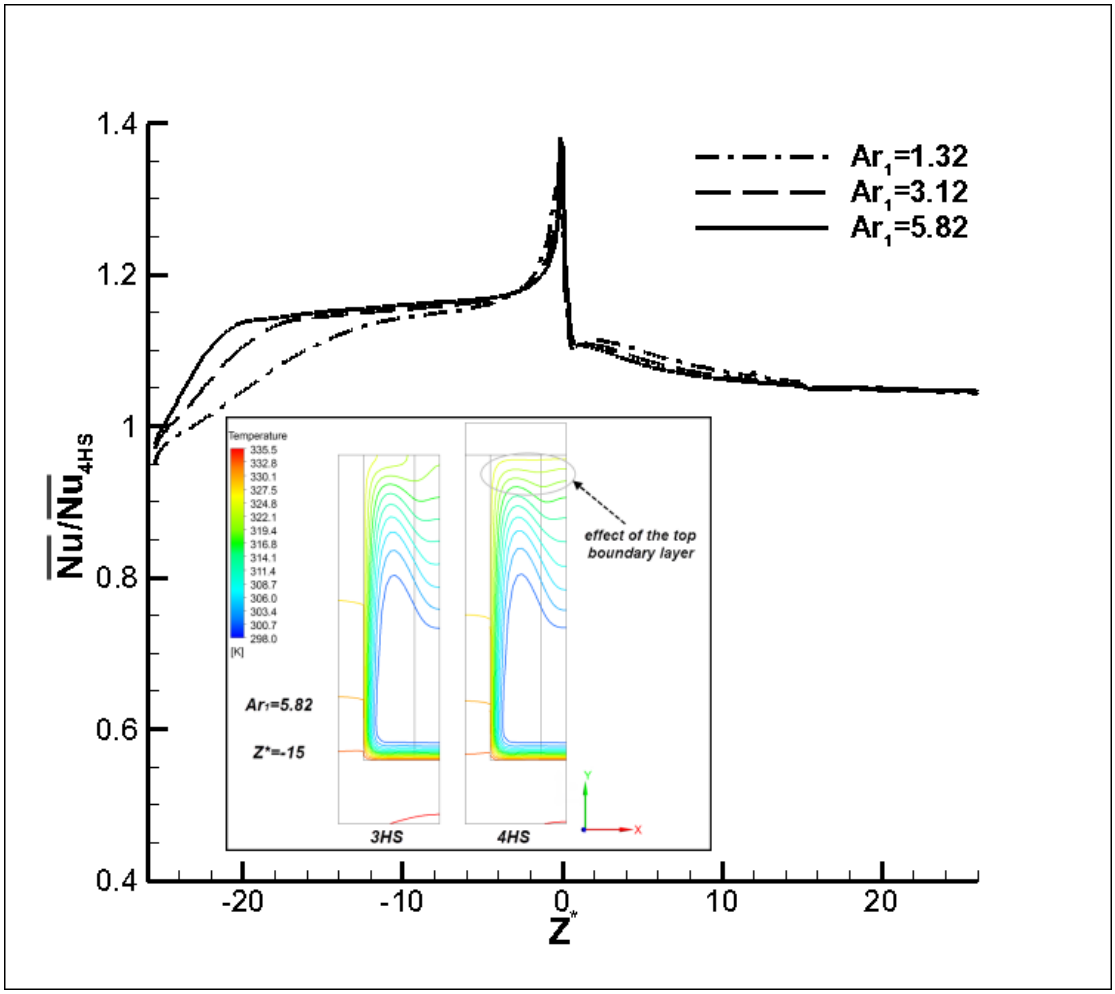

Fig.12. Comparison of the Nusselt number values attained for heating through three vs. through four surfaces.

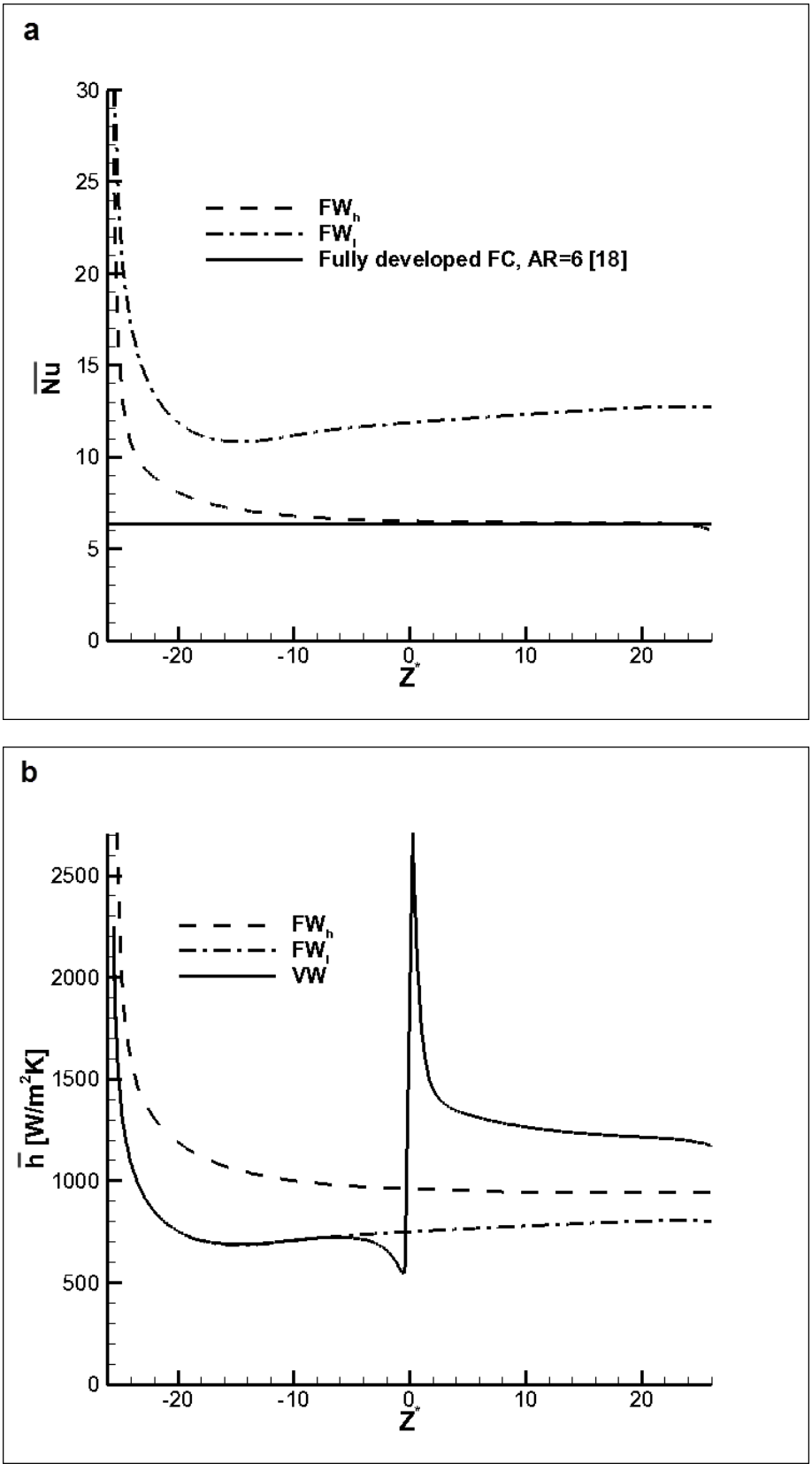

Fig.13. (a) Distribution of the average Nusselt number for the fixed-width configurations, (b) distribution of the average heat transfer coefficient.